


## Article

# Enhancing the Ethynylation Performance of CuO-Bi<sub>2</sub>O<sub>3</sub> Nanocatalysts by Tuning Cu-Bi Interactions and Phase Structures

Zhipeng Wang <sup>1</sup>, Zhuzhu Niu <sup>1</sup>, Quantai Hao <sup>1</sup>, Lijun Ban <sup>1</sup>, Haitao Li <sup>1,\*</sup>, Yongxiang Zhao <sup>1,\*</sup> and Zheng Jiang <sup>1,2</sup> 

<sup>1</sup> Engineering Research Center of Ministry of Education for Fine Chemicals, School of Chemistry and Chemical Engineering, Shanxi University, Taiyuan 030006, China; zhipengw44@163.com (Z.W.); niuzhuzhu163@163.com (Z.N.); cui602078051@163.com (Q.H.); banlijun1992@163.com (L.B.); z.jiang@soton.ac.uk (Z.J.)

<sup>2</sup> Faculty of Engineering and the Environment, University of Southampton, Highfield, Southampton SO17 1BJ, UK

\* Correspondence: htli@sxu.edu.cn (H.L.); yxzhao@sxu.edu.cn (Y.Z.); Tel.: +86-138-3457-8761 (H.L.)

Received: 29 November 2018; Accepted: 25 December 2018; Published: 2 January 2019



**Abstract:** Catalytic systems consisting of copper oxide and bismuth oxide are commonly employed for the industrial production of 1,4-butanediol (BD) through ethynylation. However, few studies have investigated the influence mechanism of Bi for these Cu-based catalysts. Herein, a series of nanostructured CuO-Bi<sub>2</sub>O<sub>3</sub> catalysts were prepared by co-precipitation followed by calcination at different temperatures. The obtained catalysts were applied to the ethynylation reaction. The textural and crystal properties of the catalysts, their reduction behavior, and the interactions between copper and bismuth species, were found to strongly depend on temperature. When calcined at 600 °C, strong interactions between Cu and Bi in the CuO phase facilitated the formation of highly dispersed active cuprous sites and stabilized the Cu<sup>+</sup> valency, resulting in the highest BD yield. Bi<sub>2</sub>O<sub>3</sub> was completely absent when calcined at 700 °C, having been converted into the spinel CuBi<sub>2</sub>O<sub>4</sub> phase. Spinel Cu<sup>2+</sup> was released gradually to form active Cu<sup>+</sup> species over eight catalytic cycles, which continuously replenished the decreasing activity resulting from the formation of metallic Cu and enhanced catalytic stability. Moreover, the positive correlation between the in-situ-formed surface Cu<sup>+</sup> ions and BD yield suggests that the amount of Cu<sup>+</sup> ions is the key factor for ethynylation of formaldehyde to BD on the as prepared CuO-Bi<sub>2</sub>O<sub>3</sub> catalysts. Based on these results and the literature, we propose an ethynylation reaction mechanism for CuO-based catalysts and provide a simple design strategy for highly efficient catalytic CuO-Bi<sub>2</sub>O<sub>3</sub> systems, which has considerable potential for industrial applications.

**Keywords:** CuO-Bi<sub>2</sub>O<sub>3</sub>; calcination temperature; ethynylation; interactions; spinel Cu<sup>2+</sup>

## 1. Introduction

In the early 1900s, Alexei Favorskii first reported the addition of alkynes to carbonyl compounds in basic media to form alkinols, which was then further developed into a known reaction process by Reppe [1]. Today, the Reppe process is the major route for the commercial manufacture of 1,4-butanediol (BD) [2,3]. Due to the numerous applications of chemicals derived from BD, such as 1,4-butanediol (BDO), 3-butene-1-ol (BTO), tetrahydrofuran (THF), poly(tetramethylene ether) glycol (PTMEG),  $\gamma$ -butyrolactone (GBL), and poly(butylene succinate) (PBS), among others [4–6], which are in high demand in the chemical, polymer, pharmaceuticals, and textiles industries [7–11], the design of highly efficient ethynylation catalysts for the synthesis of BD is of great significance.

To date, catalyst systems for the Reppe process have been reported to mainly include organic-Li, Lewis acids, and CuO-based catalysts [1,12,13]. Among them, CuO and the corresponding compounds have been widely employed due to their low costs, high activities, ease of separation from products, and their low environmental toxicities. However, active cuprous species (cuprous acetylides) generated in situ during the reaction process actually catalyze the reaction [1]. The phase transformation from CuO to the active cuprous species involves reduction and carbonization processes [14,15]. During the phase transformation, the selective reduction of  $\text{Cu}^{2+}$  to  $\text{Cu}^+$  without the formation of inactive metallic Cu while maintaining highly dispersed cuprous species is a challenging task, the outcome of which have a critical effect on the catalytic performance [16–20]. From the perspective of developing highly efficient catalysts, researchers in early studies screened catalyst components and found that CuO-based catalysts that use Bi as a promoter exhibited high activities and stabilities. Thereafter, catalysts supported by diatomite, silica gel, and  $\text{SiO}_2$ -MgO complexes and so forth, as well as synthetic malachite catalysts based on the Cu–Bi catalytic system have often been reported in the literature [21–24]. Studies have shown that the introduction of supports and/or promoters is an effective strategy for improving the ethynylation activity of Cu-based catalysts [16–24]. Despite considerable effort toward the development of Cu-based ethynylation catalysts, to the best of our knowledge, very little work has been carried out to unfold the promotion mechanism of Bi species in the ethynylation reaction and to establish the structure-activity relationships of the catalysts.

In recent years, our research group has carried out in-depth studies into the design and development of new Cu-based ethynylation catalysts, such as the  $\text{CuO-Bi}_2\text{O}_3/\text{SiO}_2\text{-MgO}$  aerogel catalyst, the  $\text{CuO-Bi}_2\text{O}_3/\text{Fe}_3\text{O}_4\text{-SiO}_2\text{-MgO}$  magnetic catalyst, and the  $\text{CuO-Bi}_2\text{O}_3@\text{SiO}_2$  core-shell catalyst [16–19]. We found that doping with specific amounts of bismuth oxide not only disperses the cuprous species, but also effectively restricts the formation of metallic Cu [2,3,12,18,19], which is consistent with previous literature reports. We speculated that interactions between Cu and Bi influence the phase transformation of CuO and, as a consequence, the catalytic performance. However, this hypothesis lacks detailed experimental evidence, especially the support of characterization data. In addition, catalytic systems constructed following previous reports or in our group are relatively complex and often include multiple components in addition to Cu and Bi, which are not conducive to clarifying the specific mechanism involving Bi on Cu. Therefore, it is necessary to simplify this complex multiple-component system to a binary Cu–Bi model catalyst.

It is important to effectively tune the structure and Cu–Bi interactions of a binary catalyst in order to systematically study the effects of Bi in Cu-based ethynylation catalysts. Numerous studies over many years have investigated the structures and performance of copper-based catalysts for methanol steam reforming, CO oxidation, carbonyl hydrogenation, etc. [25–28]. The preparation process, especially calcination temperature, has been shown to greatly impact particle size, the crystalline phase, and the interactions between different components in the catalyst, which can substantially affect catalytic performance [25–28]. Therefore, it is reasonable to expect that the calcination temperature influences the structure and the interactions between Cu and Bi in a Cu/Bi-based catalyst.

With the above discussion in mind and aided by simple calcination treatments, in the present study we investigated the structure, texture, phase transformation, and catalytic performance of binary  $\text{CuO-Bi}_2\text{O}_3$ . The relationship between structure and catalytic performance of the  $\text{CuO-Bi}_2\text{O}_3$  catalysts is discussed based on characterization studies that include Brunauer–Emmett–Teller (BET) surface-area experiments, X-ray diffraction (XRD), Raman spectroscopy, temperature-programmed reduction ( $\text{H}_2$ -TPR) studies, X-ray photoelectron spectroscopy (XPS), and CO-adsorbed infrared (CO-IR) spectroscopy. The results revealed that there are various degrees of interaction between the copper and bismuth species among catalysts calcined at different temperatures, and the formation of a spinel  $\text{CuBi}_2\text{O}_4$  phase was observed, which greatly influences catalytic activity and stability, and supplements the theoretical basis for the development of highly efficient ethynylation catalysts.

## 2. Results

### 2.1. Characterizing Fresh Catalysts

#### 2.1.1. Structure, Texture, and Morphology

To demonstrate the structural evolution, XRD patterns of fresh catalysts are displayed in Figure 1, along with that of pure CuO-600 for comparison. Here “CB” refers to the copper–bismuth catalyst and the number refers to the calcination temperature. Peaks observed at  $32.6^\circ$ ,  $35.6^\circ$ ,  $38.7^\circ$ ,  $48.8^\circ$ ,  $53.5^\circ$ ,  $58.3^\circ$ ,  $61.5^\circ$ ,  $66.2^\circ$ , and  $68.1^\circ$  in the XRD pattern of CuO are assigned to CuO (110), (002), (111), ( $-202$ ), (020), (202), ( $-113$ ), ( $-311$ ), (220), and (004) diffractions, respectively (JCPDS45-0937). In addition, a small peak at  $27.7^\circ$ , which is attributed to  $\text{Bi}_2\text{O}_3$  (121) diffraction (JCPDS41-1449), is also observed in the case of CB-500 [29]. Calcination at  $600^\circ\text{C}$  resulted in dramatic increases in the intensities of the CuO and  $\text{Bi}_2\text{O}_3$  XRD peaks. In addition, the weak peaks observed at  $28.1^\circ$  and  $33.2^\circ$  are assigned to  $\text{CuBi}_2\text{O}_4$  (211) and (102) diffractions (JCPDS48-1886), which is indicative of the formation of the spinel  $\text{CuBi}_2\text{O}_4$  phase mainly due to solid–solid interactions between CuO and  $\text{Bi}_2\text{O}_3$  [30,31]. The diffraction peaks corresponding to  $\text{Bi}_2\text{O}_3$  were entirely absent in the XRD pattern of the material calcined at  $700^\circ\text{C}$ , while the  $\text{CuBi}_2\text{O}_4$  diffraction peaks were noticeably more intense.

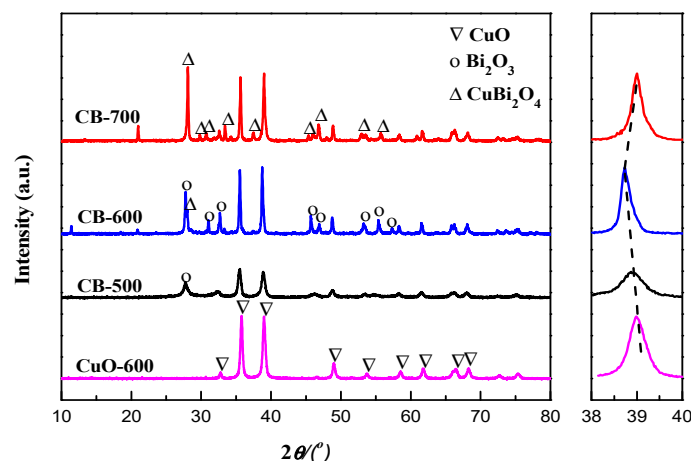


**Figure 1.** X-ray diffraction patterns (XRD) of the catalysts in this study.

The CuO crystallite sizes, calculated from the line broadening of the most intense XRD reflections using the Scherrer equation, are listed in Table 1. As the calcination temperature was increased from  $500^\circ\text{C}$  to  $600^\circ\text{C}$ , the CuO-particle size sharply increased from 17.2 to 33.0 nm. However, elevating the temperature to  $700^\circ\text{C}$  resulted in only a further slight increase in the CuO particle size, to 39.4 nm, indicating that the gradual formation of  $\text{CuBi}_2\text{O}_4$  inhibits the further growth of CuO crystals to some extent.

**Table 1.** Structural and textural data for the CuO- $\text{Bi}_2\text{O}_3$  catalysts.

Sample	$d_{\text{CuO}}$ (nm)	$S_{\text{BET}}$ ( $\text{m}^2 \text{g}^{-1}$ )		$A_{\text{Cu}^+}$ (a.u.)
		Fresh	Used	
CB-500	17.2	34.2	11.2	2.5
CB-600	33.0	20.1	13.9	2.8
CB-700	39.4	8.7	5.9	1

Note:  $d_{\text{CuO}}$  values were calculated from CuO(111) XRD reflections by the Scherrer equation;  $S_{\text{BET}}$  values for the fresh and used catalysts were calculated by the Brunauer–Emmett–Teller (BET) method; and  $A_{\text{Cu}^+}$  values were calculated using the integrated areas of  $\text{Cu}^{1+}$ -CO IR bands.

Taking the CuO(111) diffraction peak at about  $38.9^\circ$  as an example, this peak in the patterns of the CB-500 and CB-600 samples is shifted to lower diffraction angles compared to that of pure CuO-600, to  $2\theta$  values of about  $38.8^\circ$  and  $38.7^\circ$ , respectively. These observations indicate that  $\text{Bi}^{3+}$  ions thermally diffuse into the CuO crystal lattice during calcination at  $500^\circ\text{C}$  and  $600^\circ\text{C}$ . Based on their ionic radii ( $\text{Bi}^{3+}$  0.96 Å,  $\text{Cu}^{2+}$  0.72 Å), we infer that the  $\text{Bi}^{3+}$  ions doped into the CuO crystal structure in two ways, namely through substitutional and interstitial doping. Both ways expand the cell volume of the CuO crystal [32], which suggests that Cu and Bi interact. The XRD patterns reveal that the CuO in CB-600 exhibits the maximum cell volume, which demonstrates the existence of stronger Cu–Bi interactions in the CuO of the CB-600 catalyst compared to the others. Interestingly, the CuO(111) peak shifted to the same position as that observed for pure CuO in the case of CB-700, suggestive of a lack of interaction between the Cu and Bi in the CuO phase in this catalyst.

Figure 2 shows Raman spectra of fresh CuO- $\text{Bi}_2\text{O}_3$  catalysts and pure CuO-600. Three peaks—at about  $293.3\text{ cm}^{-1}$  ( $\text{A}_g$  mode),  $345.4\text{ cm}^{-1}$  ( $\text{B}_g$  mode), and  $626.4\text{ cm}^{-1}$  ( $\text{B}_g$  mode)—in pure CuO-600 are attributed to the vibrations of the oxygen atoms in the lattice (Cu–O and Cu–O–Cu bonds) [33,34]. Compared with pure CuO, the Raman peaks of CB-500 and CB-600 were broader and shifted to lower frequencies; the main peak at  $293.3\text{ cm}^{-1}$  observed for pure CuO shifted to  $293.0\text{ cm}^{-1}$  for CB-500, and to  $284.5\text{ cm}^{-1}$  for CB-600. The red-shifting and broadening of the peaks in the Raman spectra are mainly ascribable to defects in CuO originating from interactions between Cu and Bi [35,36]. Combining this information with the XRD results, we ascertain that  $\text{Bi}^{3+}$  ions diffuse into the CuO lattice to distort the CuO structure. Since a charge difference exists between  $\text{Bi}^{3+}$  and  $\text{Cu}^{2+}$ , the introduction of Bi generates oxygen vacancies in the CuO lattice to balance the charge [35,36]. Compared to CB-500, the CuO peaks in the spectrum of CB-600 were observed at lower frequencies, indicating the existence of stronger interactions in the CB-600 catalyst. No obvious Raman features corresponding to  $\text{Bi}_2\text{O}_3$  were observed in the CB-500 and CB-600 spectra, possibly due to its lower content and crystallinity. In addition, four distinct vibrational peaks—at  $130.9$ ,  $261.8$ ,  $402.8$ , and  $586.6\text{ cm}^{-1}$ —were observed for the CB-700 sample, which corresponds to the presence of  $\text{CuBi}_2\text{O}_4$  [30,31].

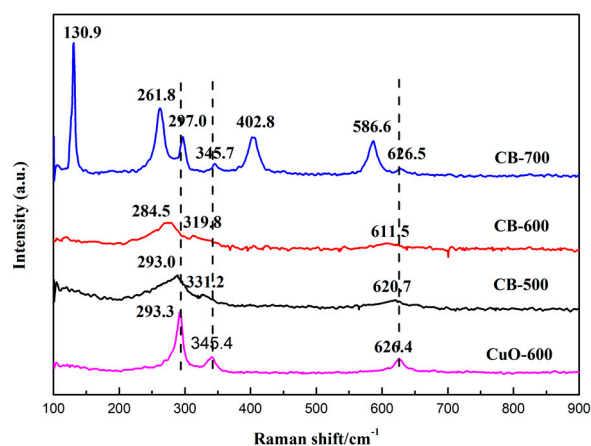
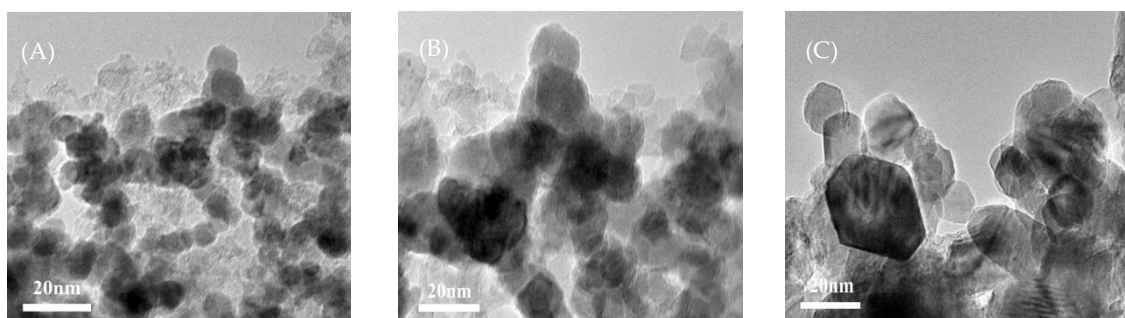


Figure 2. Raman spectra of the CuO- $\text{Bi}_2\text{O}_3$  catalysts in this study.

Table 1 presents the BET specific surface areas of the fresh catalysts. CB-500 exhibits the largest surface area ( $23.2\text{ m}^2\text{ g}^{-1}$ ); however, a significantly reduced surface area ( $8.7\text{ m}^2\text{ g}^{-1}$ ) was obtained for the sample calcined at  $700^\circ\text{C}$ . This decrease in surface area is normally associated with the growth of larger particles [27].

The morphologies and microstructures of the fresh catalysts were investigated by transmission electron microscopy (TEM). As shown in Figure 3, the catalysts have nearly spherical or irregular polyhedral morphologies. Elevated calcination temperatures lead to larger catalyst particles that are randomly distributed, which is ascribable to metal oxide sintering at high temperatures.



**Figure 3.** Transmission electron microscopy (TEM) images of the CuO-Bi<sub>2</sub>O<sub>3</sub> catalysts. (A) CB-500, (B) CB-600, and (C) CB-700.

### 2.1.2. X-ray Photoelectron Spectroscopy

The fresh CuO-Bi<sub>2</sub>O<sub>3</sub> catalysts were subjected to XPS in order to identify the surface chemical states of their copper species; the Cu2p XPS spectra are displayed in Figure 4. All catalysts displayed two peaks, one centered at about 933.1 eV and the other at about 955.9 eV, which are attributed to Cu2p<sub>3/2</sub> and Cu2p<sub>1/2</sub>, respectively. The main Cu2p<sub>3/2</sub> peak at 933.1 eV and its satellite at about 940–945 eV are characteristic of Cu<sup>2+</sup> species [37,38]. Major Cu2p<sub>3/2</sub> peaks are observed at around 933.1 eV in the spectra of CB-500 and CB-700; however, this peak was observed at 933.9 eV in the spectrum of CB-600. The positive binding-energy (BE) shifts suggest charge transfer from the metal ions to other components, which is indicative of strong interactions between Cu and Bi [39,40]. In addition, the shoulder peak at 936.0 was observed to gradually increase with increasing calcination temperature, which is attributed to spinel Cu<sup>2+</sup> species [26].

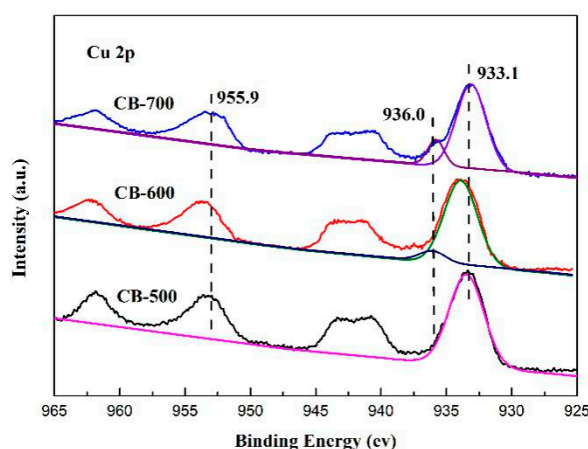


**Figure 4.** X-ray photoelectron spectroscopy (XPS) spectra of fresh and used CB-600 catalysts.

### 2.1.3. Reduction Behavior

To investigate the interactions between the different components, we employed H<sub>2</sub>-TPR experiments. As shown in Figure 5, the reduction profiles can be divided into  $\alpha$  (around 220–450 °C),  $\beta$  (around 450–550 °C), and  $\gamma$  (around 550–700 °C) peaks. The  $\alpha$  peak is attributed to the reduction of CuO. The stepwise reduction of CuO, i.e., Cu<sup>2+</sup> to Cu<sup>+</sup> (low temperature) and Cu<sup>+</sup> to Cu<sup>0</sup> (high temperature) [41,42], can be discounted because of the fast H<sub>2</sub> flow rate and deviations from the ideal pattern (the area of the low-temperature reduction peak is ideally equal to that of the high-temperature peak). The  $\alpha$  peak was observed to shift toward higher temperatures with increasing calcination temperature. In the present experiment, both increases in CuO-particle size and interactions between copper and bismuth species improve the reduction temperature [43,44]. To identify the influence of Cu–Bi interactions, we also examined the H<sub>2</sub>-TPR of pure CuO samples (Figure 6) that were calcined at different temperatures to produce CuO particles of equivalent sizes to those of the corresponding



CuO-Bi<sub>2</sub>O<sub>3</sub>. Symmetrical reduction peaks were observed for all pure CuO samples, with reduction temperatures of 257, 326, and 390 °C. By comparing the shapes and temperatures of the reduction peaks for the CB-500 and CB-600 catalysts, we ascribe the first peak—centered at about 266 °C or 339 °C—to the reduction of isolated bulk CuO and/or weak interactions between the CuO and Bi species [39], and the second peak—centered at about 334 °C or 385 °C—to the reduction of CuO that strongly interacts with Bi<sub>2</sub>O<sub>3</sub> [43,44]. Clearly, the peak area corresponding to strong CuO-Bi<sub>2</sub>O<sub>3</sub> interactions is larger in the CB-600 profile than the CB-500 profile, suggesting that stronger interaction exist within CB-600. The reduction profile of CuO-700 is very close to that of the CB-700 catalyst. Moreover, the XRD and Raman results reveal that large CuO particles devoid of interactions are observed in the CB-700 sample. Hence, the single symmetrical peak observed at 392 °C in the profile of the CB-700 catalyst is attributable to the reduction of large CuO particles. These observations suggest that calcination temperature affects the interactions between Cu and Bi and, as a consequence, the reduction behavior of the Cu species. This also illustrates that the reducibility of copper species is hindered by proper interactions between the Cu and Bi species, which might protect the copper species against further reduction by HCHO in the ethynylation reaction.

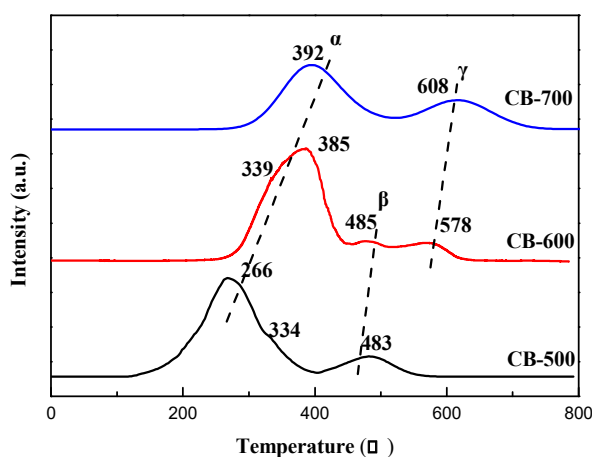


Figure 5. H<sub>2</sub>-TPR profiles of CuO-Bi<sub>2</sub>O<sub>3</sub> catalysts.

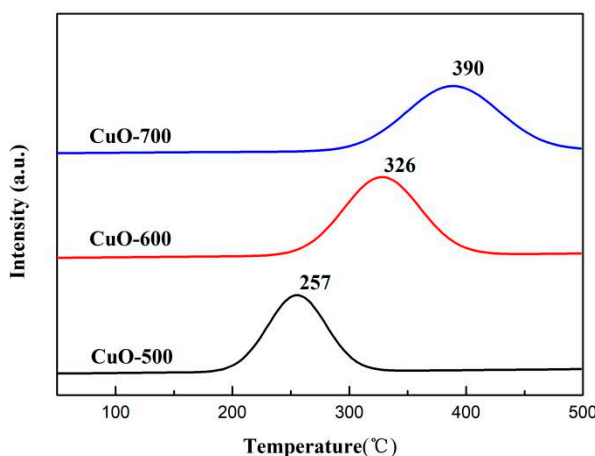


Figure 6. H<sub>2</sub>-TPR profiles of pure CuO catalysts.

These reduction properties may be related to the coordination structures and electron charge densities (ECDs) of the copper species [45,46]. The partial incorporation of Bi<sup>3+</sup> into the CuO lattice (the Cu<sup>2+</sup> ions are at centers of inversion symmetry in a single four-fold 4c site [47]) results in structural distortion, based on the above XRD and Raman results; hence, the Cu<sup>2+</sup>-coordination structures will also be distorted [32,33]. Moreover, the XPS results reveal that copper species that interact with the bismuth species exhibit higher BEs, indicating that the copper species have low outer-shell electron

densities. This result may explain why the copper species that interact with bismuth species are more difficult to reduce than bulk CuO under identical conditions. The above two points may be related to the intrinsic nature of Cu–Bi interactions.

In the higher-temperature region ( $>450\text{ }^{\circ}\text{C}$ ), the  $\beta$  and  $\gamma$  peaks mark the reductions of  $\text{Bi}_2\text{O}_3$  and  $\text{CuBi}_2\text{O}_4$ , respectively [29–31]. Compared to that of the CB-500 sample, the  $\beta$ -reduction-peak area of CB-600 was lower and a  $\gamma$  peak at  $578\text{ }^{\circ}\text{C}$  emerged due to the partial transformation of  $\text{Bi}_2\text{O}_3$  into  $\text{CuBi}_2\text{O}_4$ . The  $\gamma$  peak was even larger and shifted to a slightly higher temperature ( $608\text{ }^{\circ}\text{C}$ ) in the profile of CB-700, while the  $\beta$  peak was absent, suggesting that  $\text{Bi}_2\text{O}_3$  had completely transformed into  $\text{CuBi}_2\text{O}_4$ , with larger particles, which is consistent with the XRD results. Clearly, the  $\text{Cu}^{2+}$  species in the spinel matrix are less reducible than those in the non-spinel CuO phase. Previous authors have also observed similar phenomena in Cu–Al spinel catalysts [26,48].

In comparison to CB-500 and CB-700, CB-600 contains more copper species that interact with bismuth, which may facilitate the effective conversion of CuO into active cuprous species, thereby enhancing its catalytic performance. It should be noted that CB-700 contains more spinel copper species that seem to play crucial roles in the catalytic stability, as discussed below.

## 2.2. Characterizing the Used Catalysts

### 2.2.1. Structure and Texture

Cuprous species (cuprous acetylides) are considered to be the active species in the ethynylation reaction, which are formed in situ from CuO during the reaction [1]. These species undergo phase transformations including reduction from  $\text{Cu}^{2+}$  to  $\text{Cu}^+$  followed by coordination to acetylene. Hence, we employed XRD, BET, and CO-IR techniques to trace the changes in the structures, textures, and surface valencies of the used catalysts. Herein, we characterize the CuO– $\text{Bi}_2\text{O}_3$  catalysts after 15 h of evaluation.

The XRD patterns of the used samples shown in Figure 7 exhibit distinct diffraction-peak differences. No diffraction peaks related to CuO are observed in the pattern of CB-600. Meanwhile, weak broad peaks at about  $28.1^{\circ}$ ,  $33.0^{\circ}$ , and  $46.9^{\circ}$  emerged, which may belong to amorphous active cuprous species, which indicates that these active cuprous species form during the complete transformation of CuO and the less-crystalline  $\text{CuBi}_2\text{O}_4$  during ethynylation, which is beneficial for increased activity [16,17]. With the exception of the weak broad peaks, a diffraction peak of metallic Cu (JCPDS04-0836) was detected at a  $2\theta$  value of  $43.3^{\circ}$  for CB-500, indicating that  $\text{Cu}^{2+}$  ions were partially reduced to metallic Cu by HCHO in the ethynylation reaction [16,17]. Based on the  $\text{H}_2$ -TPR profiles of the fresh catalysts, the appearance of metallic Cu can be ascribed to noninteracting copper species, which are easily reduced in the CB-500 catalyst. In contrast, some of the CuO and  $\text{CuBi}_2\text{O}_4$  XRD peaks remained in the pattern of the CB-700 sample, suggesting that this catalyst was not completely transformed into active cuprous species because of the weak reducibility of the copper species in the large CuO particles and spinel matrices.

BET data for the used catalysts are listed in Table 1. Compared to the corresponding fresh catalysts, the surface areas of the used catalysts were all lower to various extents. This observation is possibly ascribable to the collapse of porous channels and shrinkage of the frameworks of copper oxide species during phase transformation [14,15]. The used CB-600 catalyst shows a minimal decrease in  $S_{\text{BET}}$ , suggesting that strong Cu–Bi interactions effectively hinder the migration and aggregation of catalyst particles, and retain the original framework of the fresh catalysts to an extent. Moreover, the used CB-600 also exhibits the maximal  $S_{\text{BET}}$ , which is beneficial for exposing active sites.

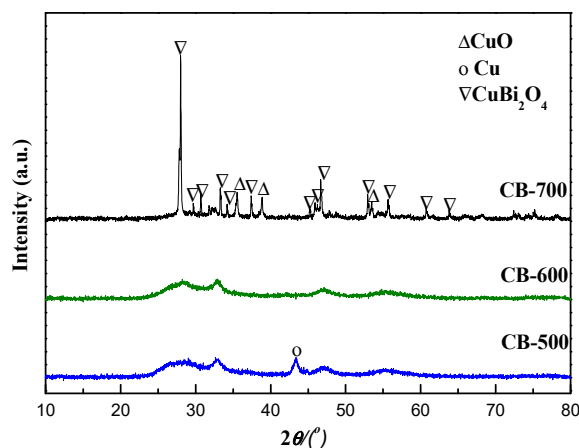


Figure 7. XRD pattern of used  $\text{CuO-Bi}_2\text{O}_3$  catalysts.

### 2.2.2. CO-IR Spectroscopy

To further determine the valencies and chemical environments of the surface copper species, CO-IR spectra were recorded and are shown in Figure 8. As detailed previously, the linear adsorption of CO on  $\text{Cu}^+$  species gives rise to peaks with vibrational frequencies at about  $2160\text{--}2110\text{ cm}^{-1}$  [49–54]. However,  $\text{Cu}^0\text{--CO}$  and  $\text{Cu}^{2+}\text{--CO}$  species are usually unstable and do not exist at room temperature, especially following the evacuation process. Thus, based on our experiment conditions and literature data, we attribute the strong peak at  $2110\text{ cm}^{-1}$  to linearly adsorbed CO on  $\text{Cu}^+$ . In addition, the intensity of this peak followed the order:  $\text{CB-600} > \text{CB-500} > \text{CB-700}$ , which corresponds to the ordering of the BET specific surface areas of the used catalysts. The results of the integrated areas of the  $\text{Cu}^{1+}\text{--CO}$  band are listed in Table 1, which reveals that the used CB-600 catalyst has the highest number of exposed active  $\text{Cu}^+$  sites, which is due to strong interactions between copper and bismuth species. On the basis of the XRD and Raman results from the calcined catalysts, we conclude that  $\text{Bi}^{3+}$  ions diffuse into the CuO lattice and distort the CuO structure. Doping with bismuth species may play a role in diluting the copper species. During phase evolution, the strong interactions between the Cu and Bi species hinder the migration and aggregation of copper species to retain the framework of the fresh catalysts to some extent. The XPS and  $\text{H}_2\text{-TPR}$  results confirm that the outer shell electron configurations and the reduction behavior of  $\text{Cu}^{2+}$  are affected by bismuth-species doping regulated by calcination temperature. The XRD results for the used catalysts further confirm that the over-reduction of  $\text{Cu}^{2+}$  to metallic Cu can be effectively restrained and that the  $\text{Cu}^+$  valency is stabilized in the used CB-600 catalyst. Similar observations have been reported by Di et al. and Wen et al. [44,55], who noted that the reduction behavior and the dispersion of copper species can be regulated by altering interactions between copper species and promoters or supports.



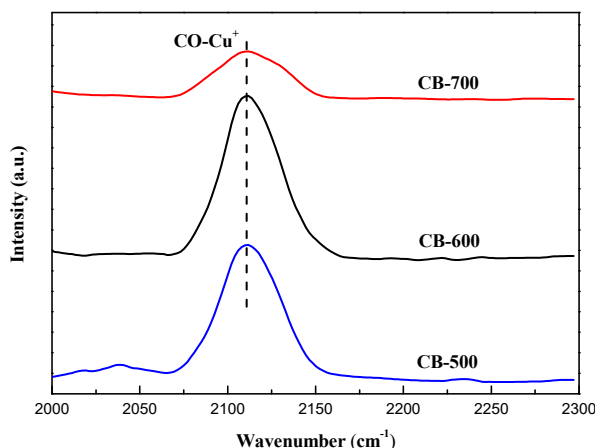
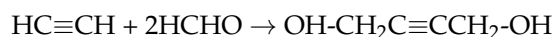


Figure 8. CO-IR spectra of used CuO-Bi<sub>2</sub>O<sub>3</sub> catalysts.

### 2.3. Catalytic Performance

The main reaction involved in the ethynylation of formaldehyde can be written as follows:



Firstly, we investigated the influence of reaction temperature on the catalytic activities of the CuO-Bi<sub>2</sub>O<sub>3</sub> and CuO catalysts in a simulated slurry reactor at 90 °C and under atmospheric pressure. The main product from the ethynylation reaction is BD; by-products, such as propargyl alcohol, formic acid, and polyformaldehyde are not shown because of their low selectivities. The yield of BD over 15 h with different reaction temperatures are plotted in Figure 9a. The reaction temperature was found to have a great influence on the catalysts performance. The yield of BD could be greatly improved with the temperature elevated. When the reaction temperature was 90 °C or 100 °C, all the catalysts displayed relatively high activity. Figure 9b displays the ethynylation activities of the CuO-Bi<sub>2</sub>O<sub>3</sub> and CuO catalysts as functions of time over 15 h at 90 °C. The CuO-based catalysts gradually became catalytic active after an induction period of around 2 h; this induction period possibly correlates with phase evolution in the catalysts. It is widely believed that cuprous acetylide is the actual active phase involved in the ethynylation reaction, rather than CuO. With extended reaction times, all catalysts showed increased activities. However, the BD yield first increased and then decreased with increasing calcination temperature. As shown in Table 1, the BD yield over CB-600 was 92.4% after 15 h. In contrast, the BD yields over CB-500 and CB-700 were 84% and 74.6% under the same conditions, respectively. Figure 10 reveals that the integrated areas of the CO-IR peaks correlate with reaction yield, which indicates that catalytic activity is proportional to the Cu<sup>+</sup> surface area and that surface cuprous species are responsible for the formation of BD.

The stabilities of the CuO-Bi<sub>2</sub>O<sub>3</sub> catalysts were examined by filtering off the catalysts after 15 h of reaction time and reusing them in another seven cycles under the reaction conditions of 90 °C and atmospheric pressure (Figure 11). The yields of BD after recycling are listed in Table 2. During the eight runs, marginal decreases in BD yield were observed for CB-600 (92.5% to 62.2%), while larger decreases were observed for CB-500 (86% to 32.8%). However, CB-700 showed optimal catalytic stability (72.5% to 65.1%), despite its lower activity. The formation of metallic Cu may be the predominant factor responsible for catalyst deactivation in this work. Hence, the CuO-Bi<sub>2</sub>O<sub>3</sub> catalysts were examined by XRD after 1, 4, and 8 cycles in order to investigate their phase evolution (Figure 12). The CB-600 and CB-500 catalysts exhibited the formation and growth of metallic Cu that positively correlates with the observed decreases in catalyst stabilities. However, metallic Cu particles were observed to grow on the CB-700 catalyst, while a decline in the CuBi<sub>2</sub>O<sub>4</sub> phase was observed after the eight runs. Hence, active cuprous species gradually formed in situ from the spinel phase, which replenished the decline in activity resulting from a decrease in Cu<sup>+</sup> species. According to the H<sub>2</sub>-TPR results, spinel Cu<sup>2+</sup>

species are more difficult to reduce than non-spinel  $\text{Cu}^{2+}$  species under the same conditions; hence, the formation of active cuprous species from the  $\text{CuBi}_2\text{O}_4$  phase will be somewhat slower than that from the  $\text{CuO}$  phase. From the above discussion, we conclude that the excellent catalytic stability of CB-700 is due to synergism between the  $\text{CuO}$  and  $\text{CuBi}_2\text{O}_4$  phases. During ethynylation, the CB-700 catalyst is first activated by the formation of active cuprous species from non-spinel  $\text{Cu}^{2+}$ , followed by the formation of active cuprous species through the gradual release of  $\text{Cu}^{2+}$  from the spinel structure, as displayed in Figure 13.

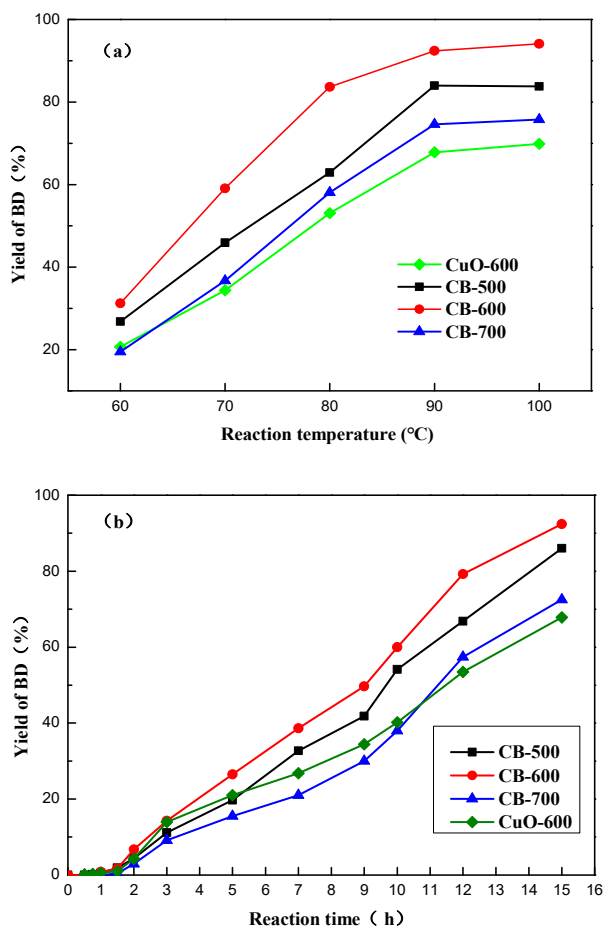


**Figure 9.** Yields of 1,4-butyne-1,3-diol (BD) over various  $\text{CuO-Bi}_2\text{O}_3$  and  $\text{CuO}$  catalysts as functions of temperature (a) and time (b).

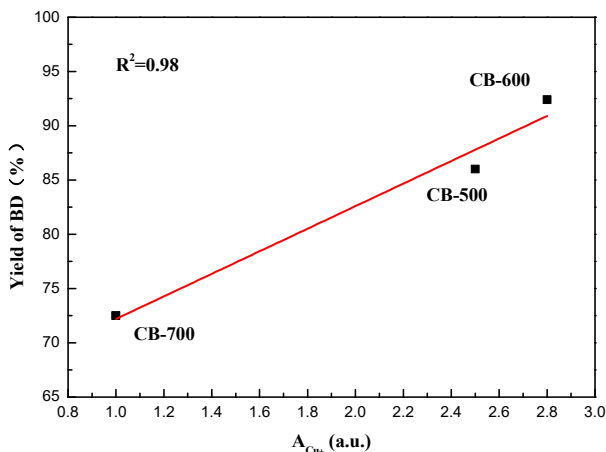


**Figure 10.** BD yield after 15 h at 90 °C as a function of the integrated area of the CO-IR peak.

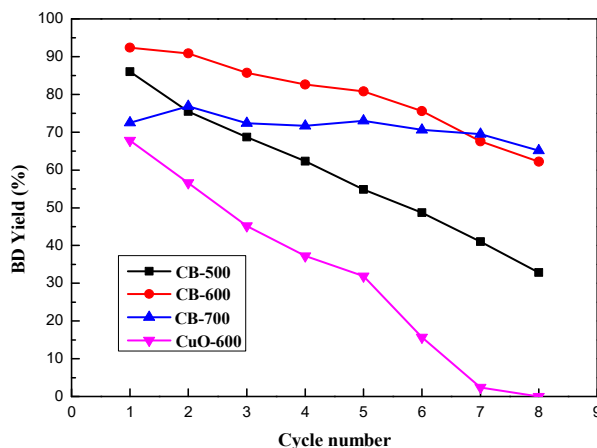


**Figure 11.** BD yields as functions of cycle number during recycling studies involving the CuO-Bi<sub>2</sub>O<sub>3</sub> and CuO catalysts.

**Table 2.** BD yields after recycling for the CuO-Bi<sub>2</sub>O<sub>3</sub> and CuO catalysts.

Sample	Y <sub>BD</sub> <sup>1</sup>	Y <sub>BD</sub> <sup>2</sup>	Y <sub>BD</sub> <sup>3</sup>	Y <sub>BD</sub> <sup>4</sup>	Y <sub>BD</sub> <sup>5</sup>	Y <sub>BD</sub> <sup>6</sup>	Y <sub>BD</sub> <sup>7</sup>	Y <sub>BD</sub> <sup>8</sup>
CB-500	86.0	75.5	68.7	62.3	54.8	48.7	41	32.8
CB-600	92.4	90.9	85.7	82.6	80.8	75.6	67.6	62.2
CB-700	72.5	76.9	72.4	71.7	73.0	70.6	69.5	65.1
CuO	67.8	56.6	45.2	37.2	31.9	15.7	2.4	0

Note: The amount of the catalyst used was 0.5 g; the concentration of the formaldehyde solution was 35 vol%; the consumption of the formaldehyde solution was 10 mL; the reaction temperature was 90 °C; the reaction time was 15 h.

Based on the above analysis, we conclude that the temperature at which the CuO-Bi<sub>2</sub>O<sub>3</sub> catalyst is calcined greatly influences its phase structure, texture, and the interactions between the metal oxide precursors, as well as the transformations of active cuprous species and the corresponding catalytic performance. There is a range of calcination temperatures at which the catalyst exhibited the best activity. The excellent catalytic performance of Cu/Bi-based catalysts is ascribable to strong interactions between Cu and Bi. On the one hand, these strong interactions stabilize the Cu<sup>+</sup> valency and inhibit the formation of metallic Cu, which facilitates the efficient transformation of CuO into active cuprous species. On the other hand, this strong interaction retains the catalyst framework and hinders the migration and aggregation of catalyst particles, resulting in more active sites exposed on the catalyst surface. In addition, the gradual release of copper species from spinel structures formed at high temperatures sustainably replenishes catalytic activity [26,56], resulting in improved catalytic stability.

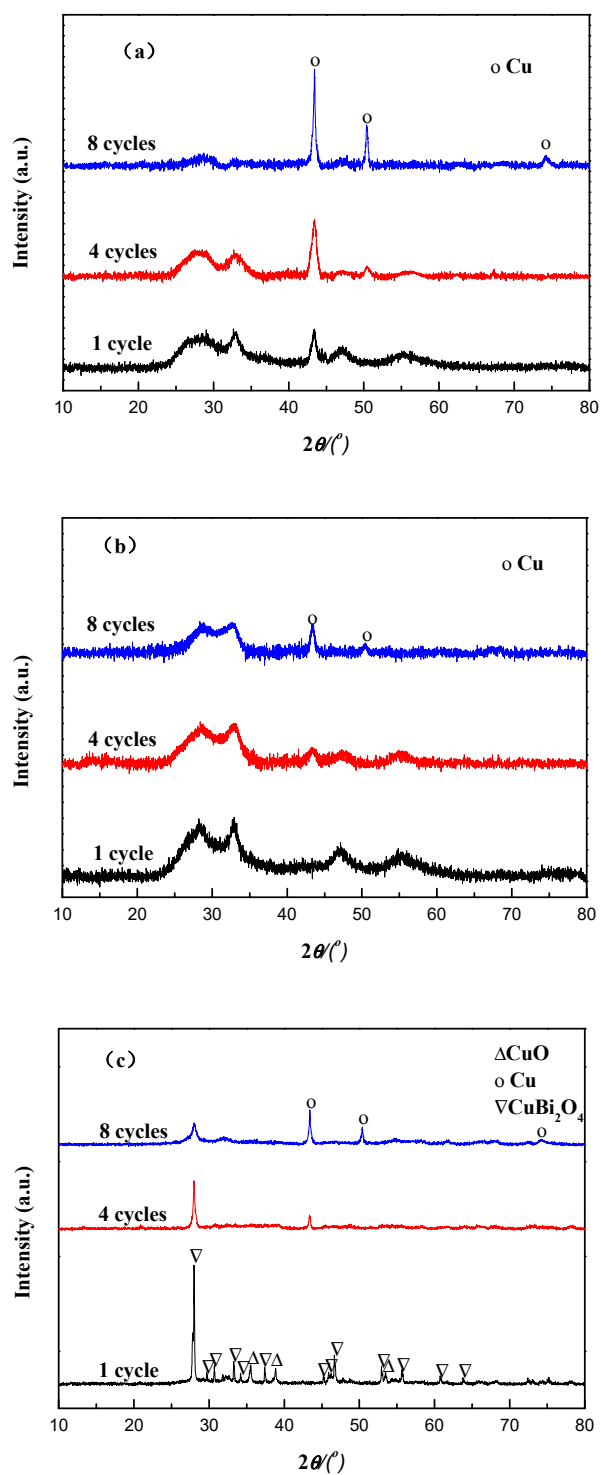


**Figure 12.** XRD patterns of the (a) CB-500, (b) CB-600, (c) CB-700 catalysts after 1, 4 and 8 recycles evaluation.

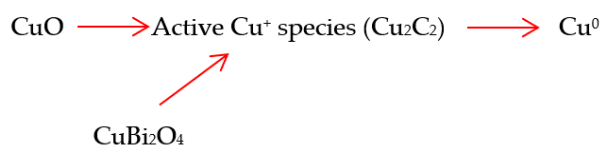


**Figure 13.** Activation process scheme of CuO and  $\text{CuBi}_2\text{O}_4$ .

## 2.4. Reaction Mechanism

Given our present observations, phase transformation appears to be important during the reaction, in which the catalysts undergo reduction and carbonization by HCHO and C<sub>2</sub>H<sub>2</sub>; this phase change can be expressed as: CuO → active cuprous species (Cu<sub>2</sub>C<sub>2</sub>) → Cu. The first phase transformation results in induction behavior that activates the catalyst. The dispersion and valence stability of Cu<sup>+</sup> species in the activated catalyst are responsible for catalytic performance. The second step deactivates the CuO-Bi<sub>2</sub>O<sub>3</sub> catalyst. The active cuprous species formed in situ are sufficiently nucleophilic to react with formaldehyde. Hübner et al. [57] also observed net electron transfer from Cu<sup>+</sup> ions in zeolites that act as electron donors to acetylene by IR spectroscopy and by quantum-chemical calculations, which demonstrated that the acetylene molecules adsorbed on the Cu<sup>+</sup> ions are nucleophilic. In contrast, it has been suggested that Cu<sup>+</sup> acts at electrophilic or Lewis acidic sites, thereby improving the reactivity of the C=O bond [39,58,59]. The carbonyl group is coordinated to Cu<sup>+</sup> through a lone pair of electrons on oxygen, leading to a more-electrophilic carbonyl carbon atom [59]. This assumption was confirmed by the hydrogenation of C=O bonds on copper-based catalysts [34]. According to the above discussion and experimental observations, we have reason to believe that the carbonyl and alkynyl are simultaneously activated by Cu<sup>+</sup> and, consequently, propose a plausible mechanism to account for the CuO-catalyzed ethynylation (Figure 14). This mechanism indirectly supports the study of Chu et al. who reported that the adsorption and activation of HCHO and C<sub>2</sub>H<sub>2</sub> molecules on catalyst surfaces are critical to the intrinsic reaction rates [60].

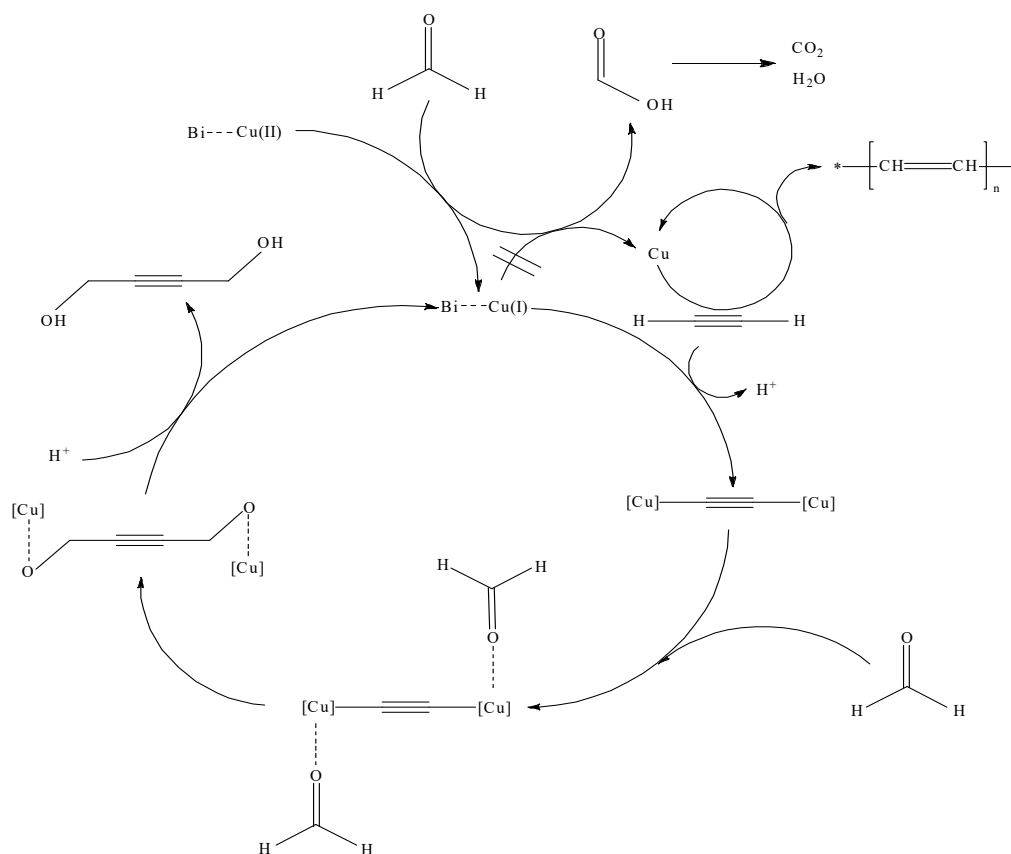


**Figure 14.** Plausible reaction mechanism for catalytic reactions involving CuO-Bi<sub>2</sub>O<sub>3</sub>.

### 3. Materials and Methods

#### 3.1. Preparation of the Catalysts

All chemical reagents, namely  $\text{Cu}(\text{NO}_3)_2$ ,  $\text{Bi}(\text{NO}_3)_3$ , PEG-400, NaOH, were of analytical grade and were used as received. The  $\text{CuO-Bi}_2\text{O}_3$  catalyst was prepared by the coprecipitation method. In a typical synthesis procedure, urea (100 g) and PEG-400 (100 g) were dissolved in 200 mL of a solution of  $\text{Cu}(\text{NO}_3)_2$  (0.5 M) and  $\text{Bi}(\text{NO}_3)_3$  (0.1 M) at room temperature. A solution of NaOH (200 mL, 2 M) was then added dropwise to the above solution at 80 °C with stirring. Following reaction, the precipitate was separated by centrifugation and washed three times (successively) with  $\text{H}_2\text{O}$  and EtOH. The final product was dried at 80 °C for 12 h and calcined at 500, 600, or 700 °C for 3 h. The powders prepared in this manner are referred to as “CB-T”, where T indicates the calcination temperature. In addition, the used catalysts were washed, filtered, and dried under vacuum at 60 °C for 48 h. Pure CuO was prepared in the same way as the  $\text{CuO-Bi}_2\text{O}_3$  samples. As summarized in Table 3, pure CuO was calcined at different temperatures to obtain samples with essentially equivalent CuO particle sizes to those of CB-500, CB-600, and CB-700. For ease of reference, these samples are referred to as “CuO-500”, “CuO-600”, and “CuO-700”, respectively.

**Table 3.** Properties of pure CuO.

Sample	Calcination Temperature (°C)	$d_{\text{CuO}}$ (nm)
CuO-500	420	16.5
CuO-600	540	35.1
CuO-700	600	40.6

Note:  $d_{\text{CuO}}$  was calculated from  $\text{CuO}(111)$  XRD reflections by the Scherrer equation.

#### 3.2. Characterization

XRD patterns were collected on a Bruker D8 Advance spectrometer (Bruker, Billerica, MA, USA) with a  $\text{Cu K}\alpha$  target ( $\lambda = 0.15418$  nm) operating at 40 kV and 40 mA, at a scanning rate of 2.4°/min and over the 10°–80°  $2\theta$  range.

$\text{N}_2$ -Physisorption analyses were performed using a Micromeritics ASAP-2020 apparatus (Norcross, GA, USA). The fresh and used samples were degassed at 150 °C for 5 h and 60 °C for 24 h respectively prior to adsorption testing. Specific surface areas were obtained using the multi-point BET procedure.

$\text{H}_2$ -TPR experiments were performed using a Micromeritics AutoChemII 2920 instrument (Norcross, GA, USA). A 30 mg sample was loaded into the instrument. A 5 vol% mixture of  $\text{H}_2$  in  $\text{N}_2$  (30 mL/min) was introduced and the temperature was raised from room temperature to 700 °C at a rate of 10 °C/min. The consumption of  $\text{H}_2$  was determined using a thermal conductivity detector, and the end gas was analyzed using an on-line quadrupole mass spectrometer (HIDEN HPR-20 QIC) (Beijing Henven Scientific Instrument Co., Ltd., Beijing, China) with a minimum dwell time of 3 ms.

Raman spectra were recorded with a LabRAM HR Evolution instrument (HORIBA, Tokyo, Japan) equipped with a CCD detector at room temperature. A 532 nm Ventus laser operating at 10 MW was used as the excitation source.

CO-IR spectra were recorded on a Bruker Tensor 27 Fourier-transform infrared spectrometer (Bruker, Billerica, MA, USA) equipped with a highly sensitive MCT detector cooled by liquid  $\text{N}_2$ . The used samples were evacuated at 60 °C for 3 h.

XPS experiments were performed in an ultra-high vacuum chamber (THERMO Scientific K-Alpha spectrometer) (Thermo Fisher Scientific, Waltham, MA, USA) at a base pressure of  $-4 \times 10^{-10}$  Torr. The XPS spectrometer was equipped with a high-resolution hemispherical electron analyzer (279.4 mm diameter with 25 meV resolution) and a  $\text{Mg K}\alpha$  ( $h\nu = 1253.6$  eV) X-ray excitation source. All spectra were referenced to adventitious C (1s) at a BE of 284.5 eV.



TEM experiments were performed using a JEOL JEM-2100 transmission electron microscope operating at 200 kV (JEOL, Tokyo, Japan). TEM samples were dispersed by sonication in ethanol followed by deposition of the suspension onto a standard Cu grid covered with a porous carbon film.

### 3.3. Catalyst Test

A 0.5 g sample of the catalyst and 10 mL of aqueous formaldehyde (30 vol%) were sequentially added to a 100-mL round bottom three-port flask equipped with a thermometer and a condenser tube. The flask was purged with N<sub>2</sub> and the system was heated to 90 °C in an oil bath with stirring, after which C<sub>2</sub>H<sub>2</sub> gas was introduced for 15 h. The mixture was cooled to room temperature following the reaction. The solid catalyst was removed by centrifugation and quantitatively analyzed on an Agilent 7890A gas chromatograph fitted with a DB-5 capillary column (0.32 mm × 50 m) and an FID detector. 1,4-Butanediol was used as the internal standard. The unconverted formaldehyde in solution was determined by iodimetry.

## 4. Conclusions

In the present study, a series of nanostructured CuO-Bi<sub>2</sub>O<sub>3</sub> catalysts was prepared using simple coprecipitation methods followed by calcination at different temperatures, after which they were applied to the ethynylation of formaldehyde to produce BD. We reveal that the calcination temperature greatly influences the crystal phase structures of the CuO-Bi<sub>2</sub>O<sub>3</sub> catalysts and interactions between the components. The CB-600 catalysts demonstrated strong interactions between CuO and Bi<sub>2</sub>O<sub>3</sub>, which improves the stability of the Cu<sup>+</sup> valence state and maintains a higher degree of dispersion of the active cuprous species during the transformation from copper oxide to cuprous acetylide, resulting in enhanced catalytic activity. The spinel CuBi<sub>2</sub>O<sub>4</sub> phase formed at high temperatures (≥600 °C) gradually releases copper species to form active cuprous species over multiple cycles, which maintains catalytic stability. Furthermore, we found a linear relationship between catalytic activity and the Cu<sup>+</sup> area, which indicates that Cu<sup>+</sup> is the actual active species that simultaneously activates C<sub>2</sub>H<sub>2</sub> and HCHO. Hence, the present observations and the literature allow us to propose a plausible ethynylation mechanism for CuO-based catalysis. Our work highlights a simple method for the rational design of highly active and stable CuO-based catalysts that simultaneously solves the problem of over-reduction and the aggregation of copper species and maintains sustainable catalysis during the phase transformation of copper oxides, thereby demonstrating important academic and industrial value.

**Author Contributions:** The idea was conceived by H.L. and Z.W. Z.W. performed the experiments and drafted the paper under the supervision of Y.Z., Z.J. and H.L. Z.N., Q.H. and L.B. helped to collect and analyse some characterization data. The manuscript was revised through the comments of all authors. All authors have given approval for the final version of the manuscript.

**Funding:** This research was funded by the National Natural Science Foundation of China (No. U1710221, 21503124) and the International Scientific and Technological Cooperation Project of Shanxi Province, China (No. 201703D421034).

**Acknowledgments:** The authors gratefully thank the financial supports of the National Natural Science Foundation of China (No. U1710221, 21503124) and the International Scientific and Technological Cooperation Project of Shanxi Province, China (No. 201703D421034).

**Conflicts of Interest:** The authors declare no conflict of interest.

## References

1. Trots, I.T.; Zimmermann, T.; Schüth, F. Catalytic reactions of acetylene: A feedstock for the chemical industry revisited. *Chem. Rev.* **2014**, *114*, 1761–1782. [[CrossRef](#)] [[PubMed](#)]
2. Reppe, W.; Keyssner, E. Production of Alkynols. U.S. Patent 2,232,867, 25 February 1941.
3. Keyssner, E.; Eichler, E. Production of Dihydric Alcohols of the Acetylene Series. U.S. Patent 2,238,471, 15 April 1941.

4. Tanielyan, S.; Schmidt, S.; Marin, N.; Alvez, G.; Augustine, R. Selective hydrogenation of 2-Butyne-1,4-diol to 1,4-Butanediol over particulate Raney<sup>®</sup> Nickel catalysts. *Top. Catal.* **2010**, *53*, 1145–1149. [[CrossRef](#)]
5. Nadgeri, J.M.; Telkar, M.M.; Rode, C.V. Hydrogenation activity and selectivity behavior of supported palladium nanoparticles. *Catal. Commun.* **2008**, *9*, 441–446. [[CrossRef](#)]
6. Kriiaa, K.; Serin, J.P.; Contamine, F.; Cézac, P.; Mercadier, J. 2-Butyne-1,4-diol hydrogenation in supercritical CO<sub>2</sub>: Effect of hydrogen concentration. *J. Supercrit. Fluids* **2009**, *49*, 227–232. [[CrossRef](#)]
7. Li, H.T.; Zhao, Y.X.; Gao, C.G.; Wang, Y.Z.; Sun, Z.J.; Liang, X.Y. Study on deactivation of Ni/Al<sub>2</sub>O<sub>3</sub> catalyst for liquid phase hydrogenation of crude 1,4-butanediol aqueous solution. *Chem. Eng. J.* **2012**, *181*–182, 501–507. [[CrossRef](#)]
8. Hari Prasad Reddy, K.; Anand, N.; Sai Prasad, P.S.; Rama Rao, K.S.; David Raju, B. Influence of method of preparation of Co-Cu/MgO catalyst on dehydrogenation/dehydration reaction pathway of 1, 4-butanediol. *Catal. Commun.* **2011**, *12*, 866–869. [[CrossRef](#)]
9. Zhang, Q.; Zhang, Y.; Li, H.T.; Gao, C.G.; Zhao, Y.X. Heterogeneous CaO-ZrO<sub>2</sub> acid-base bifunctional catalysts for vapor-phase selective dehydration of 1,4-butanediol to 3-buten-1-ol. *Appl. Catal. A Gen.* **2013**, *466*, 233–239. [[CrossRef](#)]
10. Kim, M.N.; Kim, K.H.; Jin, H.J.; Park, J.K.; Yoon, J.S. Biodegradability of ethyl and n-octyl branched poly(ethylene adipate) and poly(butylene succinate). *Eur. Polym. J.* **2001**, *37*, 1843–1847. [[CrossRef](#)]
11. Zhao, F.Y.; Ikushima, Y.; Arai, M. Hydrogenation of 2-butyne-1,4-diol in supercritical carbon dioxide promoted by stainless steel reactor wall. *Catal. Today* **2004**, *93–95*, 439–443. [[CrossRef](#)]
12. Bonrath, W.; Bernd, E.; Reinhard, K.; Schneider, M. Ethynylation Process. U.S. Patent 6,949,685, 27 September 2005.
13. Frantz, D.E.; Fässler, R.; Carreira, E.M. Facile Enantioselective Synthesis of Propargylic Alcohols by Direct Addition of Terminal Alkynes to Aldehydes. *J. Am. Chem. Soc.* **2000**, *122*, 1806–1807. [[CrossRef](#)]
14. Bukur, D.B.; Okabe, K.; Rosynek, M.P.; Li, C.P.; Wang, D.J.; Rao, K.R.P.M.; Huffman, G.P. Activation studies with a precipitated iron catalyst for Fischer-Tropsch synthesis. *J. Catal.* **1995**, *155*, 353–365. [[CrossRef](#)]
15. Gao, F.F.; Wang, H.; Qing, M.; Yang, Y.; Li, Y.W. Controlling the phase transformations and performance of iron-based catalysts in the Fischer-Tropsch synthesis. *Chin. J. Catal.* **2013**, *34*, 1312–1325. [[CrossRef](#)]
16. Wang, J.J.; Li, H.T.; Ma, Z.Q.; Wang, Z.P.; Guo, J.Y.; Zhao, Y.X. Preparation of magnetic CuO-Bi<sub>2</sub>O<sub>3</sub>/Fe<sub>3</sub>O<sub>4</sub>-SiO<sub>2</sub>-MgO catalyst and its catalytic performance for formaldehyde ethynylation. *J. Chem. Ind. Eng.* **2015**, *66*, 2098–2104.
17. Zheng, Y.; Sun, Z.J.; Wang, Y.Z.; Li, H.T.; Wang, S.A.; Luo, M.; Zhao, J.L.; Zhao, Y.X. Preparation of CuO-Bi<sub>2</sub>O<sub>3</sub>/SiO<sub>2</sub>-MgO catalyst and its ethynylation performance. *J. Mol. Catal.* **2012**, *26*, 233–238.
18. Yang, G.F.; Li, H.T.; Zhang, H.X.; Wang, Z.P.; Liu, L.L.; Zhao, Y.X. Effect of NaOH concentration on structure and catalytic performance of Cu<sub>2</sub>O for formaldehyde ethynylation. *J. Mol. Catal.* **2016**, *30*, 540–546.
19. Li, H.T.; Niu, Z.Z.; Yang, G.F.; Zhang, H.X.; Wang, Z.P.; Zhao, Y.X. Support effect of Cu<sub>2</sub>O/TiO<sub>2</sub> employed in formaldehyde ethynylation. *J. Chem. Ind. Eng.* **2018**, *69*, 2512–2518.
20. Reppe, W.; Steinhof, A.; Spaenig, H. Production of Alkynols. U.S. Patent 2,300,969, 3 November 1942.
21. Codignola, F.; Aires, B. Process for the Catalytic Hydrogenation of 1,4-Butynediol to 1,4-Butanediol. U.S. Patent 4,438,285, 20 March 1984.
22. Hort, E.V.; Piscataway, N.J. Ethynylation Catalyst and Method of Production Alkynols by Low Pressure Reactions. U.S. Patent 3,920,759, 18 November 1975.
23. Fremont, J.M. Malachite Preparation. U.S. Patent 4,107,082, 15 August 1978.
24. Fremont, J.M. Preparation of Butynediol Using Bismuth Modified Spheroidal Malachite. U.S. Patent 4,127,734, 28 November 1978.
25. Luo, M.F.; Fang, P.; He, M.; Xie, Y.L. In situ XRD, Raman, and TPR studies of CuO/Al<sub>2</sub>O<sub>3</sub> catalysts for CO oxidation. *J. Mol. Catal. A Chem.* **2005**, *239*, 243–248. [[CrossRef](#)]
26. Liu, Y.J.; Qing, S.J.; Hou, X.N.; Qin, F.J.; Wang, X.; Gao, Z.X.; Xiang, H.W. Temperature dependence of Cu–Al spinel formation and its catalytic performance in methanol steam reforming. *Catal. Sci. Technol.* **2017**, *7*, 5069–5078. [[CrossRef](#)]
27. Zhu, Y.F.; Kong, X.; Cao, D.B.; Cui, J.L.; Zhu, Y.L.; Li, Y.W. The rise of calcination temperature enhances the performance of Cu catalysts: Contributions of support. *ACS Catal.* **2014**, *4*, 3675–3681. [[CrossRef](#)]

28. Chen, C.; Cao, J.J.; Cargnello, M.; Fornasiero, P.; Gorte, R.J. High-temperature calcination improves the catalytic properties of alumina-supported Pd@ceria prepared by self assembly. *J. Catal.* **2013**, *306*, 109–115. [\[CrossRef\]](#)
29. Abdulkarem, A.M.; Aref, A.A.; Abdulhabeeb, A.; Li, Y.F.; Yu, Y. Synthesis of Bi<sub>2</sub>O<sub>3</sub>/Cu<sub>2</sub>O nanoflowers by hydrothermal method and its photocatalytic activity enhancement under simulated sunlight. *J. Alloys Compd.* **2013**, *560*, 132–141. [\[CrossRef\]](#)
30. Muthukrishnaraj, A.; Vadivel, S.; Made Joni, I.; Balasubramanian, N. Development of reduced graphene oxide/CuBi<sub>2</sub>O<sub>4</sub> hybrid for enhanced photocatalytic behavior under visible light irradiation. *Ceram. Int.* **2015**, *41*, 6164–6168. [\[CrossRef\]](#)
31. Abdulkarem, A.M.; Li, J.L.; Aref, A.A.; Ren, L.; Elssaf, E.M.; Wang, H.; Ge, Y.K.; Yu, Y. CuBi<sub>2</sub>O<sub>4</sub> single crystal nanorods prepared by hydrothermal method: Growth mechanism and optical properties. *Mater. Res. Bull.* **2011**, *46*, 1443–1450. [\[CrossRef\]](#)
32. Qin, W.; Qi, J.; Wu, X.H. Photocatalytic property of Cu<sup>2+</sup>-doped Bi<sub>2</sub>O<sub>3</sub> films under visible light prepared by the sol-gel method. *Vacuum* **2014**, *107*, 204–207. [\[CrossRef\]](#)
33. Xu, J.F.; Ji, W.; Shen, Z.X.; Li, W.S.; Tang, S.H.; Ye, X.R.; Jia, D.Z.; Xin, X.Q. Raman spectra of CuO nanocrystals. *J. Raman Spectrosc.* **1999**, *30*, 413–415. [\[CrossRef\]](#)
34. Zhu, Y.F.; Zhu, Y.L.; Ding, G.Q.; Zhu, S.H.; Zheng, H.Y.; Li, Y.W. Highly selective synthesis of ethylene glycol and ethanol via hydrogenation of dimethyl oxalate on Cu catalysts: Influence of support. *Appl. Catal. A* **2013**, *468*, 296–304. [\[CrossRef\]](#)
35. Águila, G.; Gracia, F.; Araya, P. CuO and CeO<sub>2</sub> catalysts supported on Al<sub>2</sub>O<sub>3</sub>, ZrO<sub>2</sub>, and SiO<sub>2</sub> in the oxidation of CO at low temperature. *Appl. Catal. A* **2008**, *343*, 16–24. [\[CrossRef\]](#)
36. Águila, G.; Gracia, F.; Cortés, J.; Araya, P. Effect of copper species and the presence of reaction products on the activity of methane oxidation on supported CuO catalysts. *Appl. Catal. B* **2008**, *77*, 325–338. [\[CrossRef\]](#)
37. Sato, A.G.; Volanti, D.P.; Meira, D.M. Effect of the ZrO<sub>2</sub> phase on the structure and behavior of supported Cu catalysts for ethanol conversion. *J. Catal.* **2013**, *307*, 1–17. [\[CrossRef\]](#)
38. Zhu, S.H.; Gao, X.Q.; Zhu, Y.L.; Zhu, Y.F.; Zheng, H.Y.; Li, Y.W. Promoting effect of boron oxide on Cu/SiO<sub>2</sub> catalyst for glycerol hydrogenolysis to 1,2-propanediol. *J. Catal.* **2013**, *303*, 70–79. [\[CrossRef\]](#)
39. Yin, A.Y.; Guo, X.Y.; Dai, W.L.; Fan, K.N. The nature of active copper species in Cu-HMS catalyst for hydrogenation of dimethyl oxalate to ethylene glycol: New insights on the synergetic effect between Cu<sup>0</sup> and Cu<sup>+</sup>. *J. Phys. Chem. C* **2009**, *113*, 11003–11013. [\[CrossRef\]](#)
40. Zhang, B.; Zhu, Y.L.; Ding, G.Q.; Zheng, H.Y.; Li, Y.W. Modification of the supported Cu/SiO<sub>2</sub> catalyst by alkaline earth metals in the selective conversion of 1, 4-butanediol to  $\gamma$ -butyrolactone. *Appl. Catal. A* **2012**, *443–444*, 191–201. [\[CrossRef\]](#)
41. Xue, J.J.; Wang, X.Q.; Qi, G.S.; Wang, J.; Shen, M.Q.; Li, W. Characterization of copper species over Cu/SAPO-34 in selective catalytic reduction of NO<sub>x</sub> with ammonia: Relationships between active Cu sites and de-NO<sub>x</sub> performance at low temperature. *J. Catal.* **2013**, *297*, 56–64. [\[CrossRef\]](#)
42. Bienholz, A.; Blume, R.; Knop-Gericke, A.; Girgsdies, F.; Behrens, M.; Claus, P. Prevention of catalyst deactivation in the hydrogenolysis of glycerol by Ga<sub>2</sub>O<sub>3</sub>-modified copper/zinc oxide Catalysts. *J. Phys. Chem. C* **2011**, *115*, 999–1005. [\[CrossRef\]](#)
43. Hu, Z.P.; Zhu, Y.P.; Gao, Z.M.; Wang, G.X.; Liu, Y.P.; Yuan, Z.Y. CuO catalysts supported on activated red mud for efficient catalytic carbon monoxide oxidation. *Chem. Eng. J.* **2016**, *302*, 23–32. [\[CrossRef\]](#)
44. Wen, C.; Yin, A.Y.; Cui, Y.Y.; Yang, X.L.; Dai, W.L.; Fan, K.N. Enhanced catalytic performance for SiO<sub>2</sub>-TiO<sub>2</sub> binary oxide supported Cu-based catalyst in the hydrogenation of dimethyloxalate. *Appl. Catal. A Gen.* **2013**, *458*, 82–89. [\[CrossRef\]](#)
45. Sun, C.Z.; Zhu, J.; Lv, Y.Y.; Qi, L.; Liu, B.; Gao, F.; Sun, K.Q.; Dong, L.; Chen, Y. Dispersion, reduction and catalytic performance of CuO supported on ZrO<sub>2</sub>-doped TiO<sub>2</sub> for NO removal by CO. *Appl. Catal. B* **2011**, *103*, 206–220. [\[CrossRef\]](#)
46. Hu, Y.H.; Dong, L.; Wang, J.; Ding, W.P.; Chen, Y. Activities of supported copper oxide catalysts in the NO + CO reaction at low temperatures. *J. Mol. Catal. A Chem.* **2000**, *162*, 307–316. [\[CrossRef\]](#)
47. Zhang, Q.B.; Zhang, K.L.; Xu, D.G. CuO nanostructures: Synthesis, characterization, growth mechanisms, fundamental properties, and applications. *Prog. Mater. Sci.* **2014**, *60*, 208–337. [\[CrossRef\]](#)
48. Li, G.J.; Gu, C.T.; Zhu, W.B.; Wang, X.F.; Yuan, X.F.; Cui, Z.J.; Wang, H.L.; Gao, Z.X. Hydrogen production from methanol decomposition using Cu-Al spinel catalysts. *J. Clean. Prod.* **2018**, *183*, 415–423. [\[CrossRef\]](#)

49. Kefirov, R.; Penkova, A.; Hadjiivanov, K.; Dzwigaj, S.; Che, M. Stabilization of Cu<sup>+</sup> ions in BEA zeolite: Study by FTIR spectroscopy of adsorbed CO and TPR. *Micropor. Mesopor. Mater.* **2008**, *116*, 180–187. [[CrossRef](#)]
50. Hadjiivanov, K.; Vayssilov, G. Characterization of oxide surfaces and zeolites by carbon monoxide as an IR probe molecule. *Adv. Catal.* **2002**, *47*, 307–511.
51. Tang, Y.X.; Dong, L.H.; Deng, C.S.; Huang, M.N.; Li, B.; Zhang, H.L. In situ FT-IR investigation of CO oxidation on CuO/TiO<sub>2</sub> catalysts. *Catal. Commun.* **2016**, *78*, 33–36. [[CrossRef](#)]
52. Broclawik, E.; Kozyra, P.; Datka, J. IR studies and DFT quantum chemical calculations concerning interaction of some organic molecules with Cu<sup>+</sup> sites in zeolites. *C. R. Chim.* **2005**, *8*, 491–508. [[CrossRef](#)]
53. Datka, J.; Kukulska-Zajac, E.; Kobyzew, W. IR studies of coadsorption of organic molecules and CO on Cu<sup>+</sup> cations in zeolites. *Catal. Today* **2006**, *114*, 169–173. [[CrossRef](#)]
54. Xiong, Y.; Yao, X.J.; Tang, C.J.; Zhang, L.; Cao, Y.; Deng, Y.; Gao, F.; Dong, L. Effect of CO-pretreatment on the CuO–V<sub>2</sub>O<sub>5</sub>/γ-Al<sub>2</sub>O<sub>3</sub> catalyst for NO reduction by CO. *Catal. Sci. Technol.* **2014**, *4*, 4416–4425. [[CrossRef](#)]
55. Di, W.; Cheng, J.H.; Tian, S.X.; Li, J.; Chen, J.Y.; Sun, Q. Synthesis and characterization of supported copper phyllosilicate catalysts for acetic ester hydrogenation to ethanol. *Appl. Catal. A* **2016**, *510*, 244–259. [[CrossRef](#)]
56. Shokouhimehr, M. Magnetically separable and sustainable nanostructured catalysts for heterogeneous reduction of nitroaromatics. *Catalysts* **2015**, *5*, 534–560. [[CrossRef](#)]
57. Hübner, G.; Rauhut, G.; Stoll, H.; Roduner, E. Ethyne adsorbed on CuNaY zeolite: FTIR spectra and quantum chemical calculations. *J. Phys. Chem. B* **2003**, *107*, 8568. [[CrossRef](#)]
58. Poels, E.K.; Brands, D.S. Modification of Cu/ZnO/SiO<sub>2</sub> catalysts by high temperature reduction. *Appl. Catal. A* **2000**, *191*, 83–96. [[CrossRef](#)]
59. Gong, J.L.; Yue, H.R.; Zhao, Y.J.; Zhao, S.; Zhao, L.; Lv, J.; Wang, S.P.; Ma, X.B. Synthesis of ethanol via syngas on Cu/SiO<sub>2</sub> catalysts with balanced Cu<sup>0</sup>–Cu<sup>+</sup> Sites. *J. Am. Chem. Soc.* **2012**, *134*, 13922–13925. [[CrossRef](#)] [[PubMed](#)]
60. Chu, J.J.; Li, K.T.; Wang, I. Kinetics of the synthesis of 1,4-butanediol over a copper-bismuth/magnesium silicate catalyst. *Appl. Catal. A* **1993**, *97*, 123–132. [[CrossRef](#)]



© 2019 by the authors. Licensee MDPI, Basel, Switzerland. This article is an open access article distributed under the terms and conditions of the Creative Commons Attribution (CC BY) license (<http://creativecommons.org/licenses/by/4.0/>).